Effect of percolation in an intergrowth structure

1991 J. Phys.: Condens. Matter 3 2479

(http://iopscience.iop.org/0953-8984/3/15/003)

J. Phys.: Condens. Matter 3 (1991) 2479–2497. Printed in the UK

Effect of percolation in an intergrowth structure

K K Singh†, P Ganguly‡, P P Edwards†‖ and J B Goodenough§

† IRC in Superconductivity, West Cambridge Site, Madingley Road, Cambridge, UK

‡ Physical Chemistry Division, National Chemical Laboratory, Pune 411008, India

§ Center for Materials Science and Engineering, University of Texas at Austin, Austin, TX 78712-1084, USA

Received 14 August 1990

Abstract. The three systems $LaSrAl_{1-x}Ni_xO_4$, $LaSrAl_{1-x}Fe_xO_4$ and $LaSrFe_{1-x}Ni_xO_4$ have the tetragonal K_2NiF_4 structure and a two-dimensional percolation limit $x_c \simeq 0.59$. A tolerance factor $t > 1$ in $LaSrAlO_4$ creates a large c/a axial ratio due to relief of compressive stress in the rocksalt layer. $LaSrNiO_4$ contains low-spin Ni(III) with one itinerant $\sigma^*_{x^2-y^2}$ electron per Ni atom. *$LaSrFeO_4$ is an antiferromagnet with high-spin Fe^{3+} ions. For $x < x_c$ in* $LaSrAl_{1-x}Ni_xO_4$, the low-spin Ni(III) contains a localized $3d_{z^2}$ electron; on crossing $x \simeq x_c$, a sharp transition from a p-type to an n-type semiconductor is accompanied by a sharp change in the c/a axial ratio as the $3d_{z^2}$ and $3d_{x^2-y^2}$ energies cross. In $LaSrAl_{1-x}Fe_xO_4$, long-range antiferromagnetic order is only found for $x > x_c$. In $LaSrFe_{1-x}Ni_xO_4$, the low-spin Ni(III) ions have a $3d_{x^2-y^2}$ orbital more stable than the $3d_{z^2}$ orbital for all x, and antiferromagnetic coupling occurs for all $x < x_c$.

1. Introduction

The tetragonal A_2MX_4 structure illustrated in figure 1 is an intergrowth of two rocksalt (001) planes $(AX)_2$ alternating with MX_2 planes having 180° M—X—M bonds. Early interest in this structure concentrated on oxides X ≡ O having a transition-metal atom M because of the strongly anisotropic character of the M–O–M interactions within a basal plane versus M–O–O–M interactions between the basal planes. This strong anisotropy is manifest in the high-T_c copper oxide superconductors $La_{2-x}Sr_xCuO_4$, $0.08 \leqslant x \leqslant 0.27$ [1, 2], and $La_2CuO_{4+\delta}$ [3].

This structure is also of interest because it illustrates how nature adapts to the thermal mismatch between intergrowth layers of different thermal expansion coefficients [4]. The significance of the thermal expansion mismatch for the properties of the $La_{2-x}Sr_xCuO_{4\pm\delta}$ system has been emphasized elsewhere [5]. This paper presents the results of a preliminary exploration not only of the influence of the bond-length mismatch but also of the percolation threshold on the room-temperature properties of three solid-solution systems having the structure in figure 1: $LaSrM_{1-x}M'_xO_{4\pm\delta}$ with M, M′ ≡ Al, Fe, Ni (but M ≠ M′). The choice of $A_2 \equiv$ LaSr permits stabilization of trivalent M atoms provided that the oxygen stoichiometry can be controlled to $\delta \simeq 0$. Trivalent nickel has the low-spin configuration $t_{2g}^6e^1$ in a cubic octahedral site, which introduces a degree of freedom for the distribution of the single e electron between the two e orbitals, and the

‖ Present address: School of Chemistry, University of Birmingham, Edgbaston, Birmingham B15 2TT, UK.

0953-8984/91/152479 + 19 $03.50

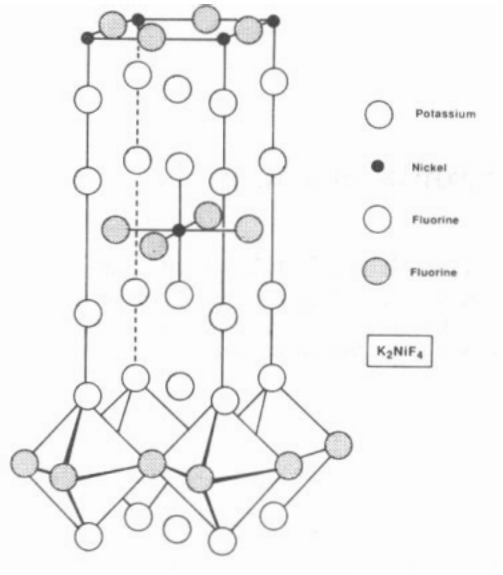

Figure 1. Crystal structure of K_2NiF_4.

spherically symmetric Al^{3+} and Fe^{3+} ions present significantly different Al–O–Ni versus Fe–O–Ni interactions.

2. Experimental details

The $LaSrAl_{1-x}Ni_xO_4$ and $LaSrFe_{1-x}Ni_xO_4$ compounds were prepared as follows. Estimated solutions of $LaCl_3$, $Sr(NO_3)_2$, $Al(NO_3)_2$, $FeCl_3$ and $NiCl_2$ were taken in the required proportions and the obtained mixture was added slowly to a hot solution of Na_2CO_3 with constant stirring. The precipitate was washed several times with hot water until the filtrate did not give any pink colour with phenolphthalein indicator. The resulting precipitate was dried and decomposed at 1170 K for 10 h, after which the powder was ground, pelletized and sintered at 1570 K for 48 h with an intermittent grinding and then heated in an O_2 atmosphere at 1570 K. The $LaSrAl_{1-x}Fe_xO_4$ were prepared from a stoichiometric mixture of $La(NO_3)_3$, $Sr(NO_3)_2$, $Al(NO_3)_3$ and $Fe(NO_3)_2$ solutions, precipitated as hydroxides using ammonia. The precipitate was first decomposed and then sintered at 1370 K in air with intermittent grinding.

The stoichiometries of these compounds were established by estimating the excess oxygen using iodometric titrations. The single phase of these samples was ascertained from their x-ray diffractograms using a Philips x-ray diffractometer PW1060/70. The magnetic susceptibilities of these compounds were measured by the Faraday method using an electromagnet with shaped pole pieces and a Cahn RG electrobalance, fitted with an air product closed-cycle Displex CS201 refrigeration unit. $HgCo(NCS)_4$ was used as the calibrant for the susceptibility studies. Mössbauer spectra of the materials was recorded at ambient temperature (293 K) on an ECIL MBS-35 spectrometer using a multichannel analyser. The spectrometer was calibrated against natural iron hyperfine spectrum. The observed linewidth ($\Gamma_{1/2}$) of natural iron was 0.19 mm s^{-1}. The spectral data was processed using a standard least-square fitting program, MOSFIT. Electrical

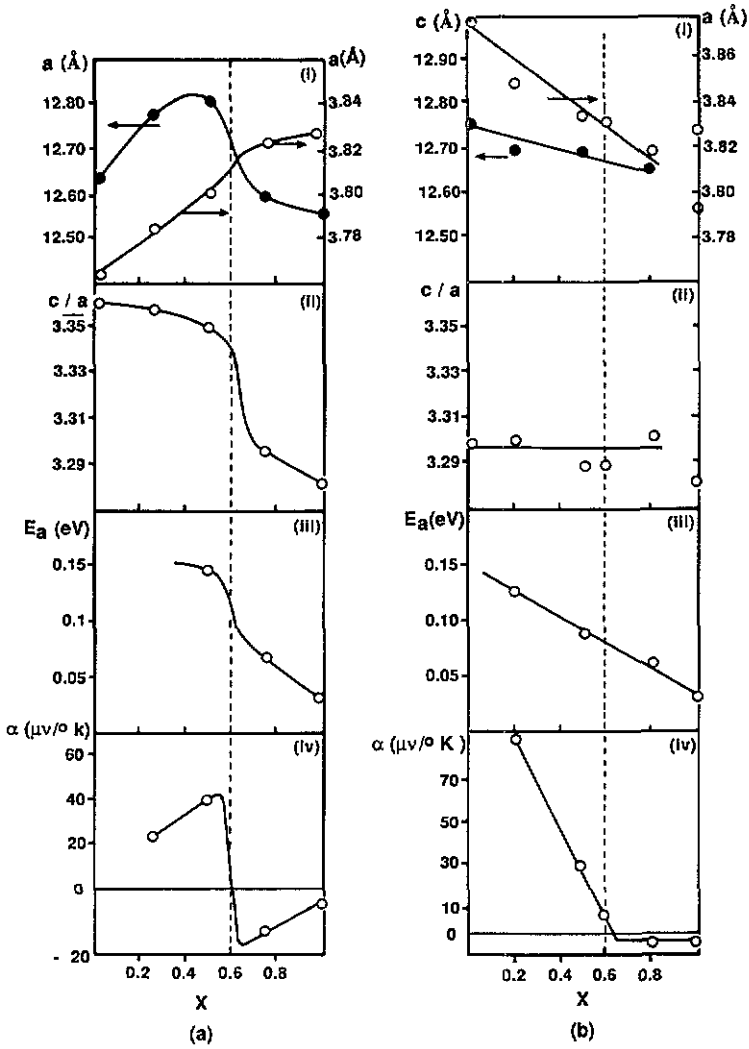

Figure 2. Variation in structural parameters (a, c and c/a) and transport parameters (E_a and α) as a function of x in the series (a) $LaSrAl_{1-x}Ni_xO_4$ and (b) $LaSrFe_{1-x}Ni_xO_4$. See text for detailed description of E_a.

resistivity measurements were made by the four-probe technique. Electron spin resonance (ESR) spectra were recorded on a Varian E-109 spectrometer. The Seebeck coefficient was measured with a home-built apparatus.

3. Results

3.1. $LaSrAl_{1-x}Ni_xO_4$

Figure 2(a) presents the room temperature lattice parameters and the corresponding c/a ratios determined by powder x-ray diffraction. Of particular interest is the strong deviation from Végard's law with a marked change in the compositional dependence

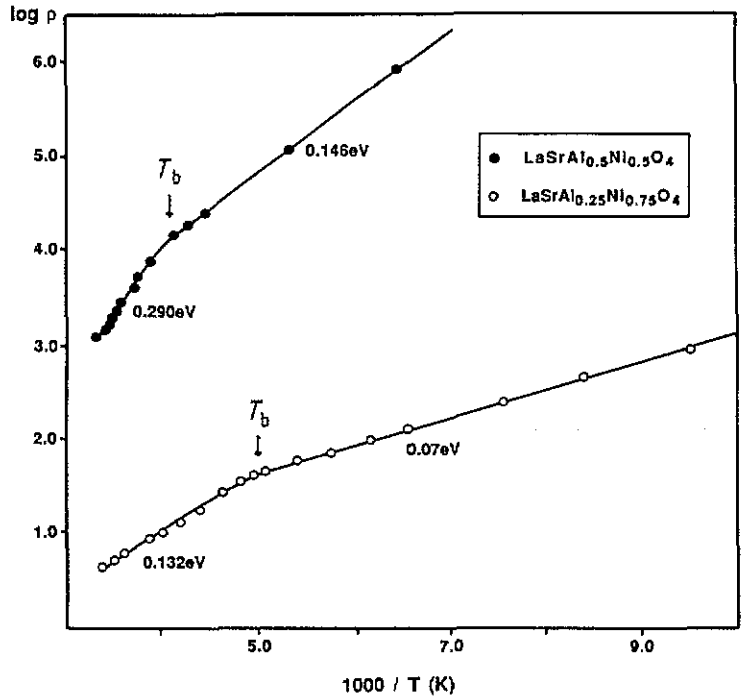

Figure 3. log ρ versus $1000/T$ plots of the $x = 0.50$ and 0.75 samples in the $LaSrAl_{1-x}Ni_xO_4$ series. T_b defined in text.

occurring within the interval $0.5 < x < 0.75$. This structural change is also reflected in the transport properties shown in figure 2(*a*). Especially striking is the abrupt change in the sign of the Seebeck coefficient α in the interval $0.5 < x < 0.75$.

Figure 3 shows the temperature dependence of the logarithm of the resistivity for samples $x = 0.5$ and 0.75 in the $LaSrAl_{1-x}Ni_xO_4$ series. A high room-temperature resistivity ($\rho > 10^6\ \Omega$ cm) for $x = 0.05$ and 0.25 prevented comparable measurements on these samples. The low-temperature activation energies E_a obtained from $\rho = \rho_0 \exp(E_a/kT)$ are shown in figure 2(*a*)(iii) and compared in table 1 with the high-temperature activation energies. The temperature at which the slopes of the curves in figure 3 change is defined as the break temperature T_b.

Figure 4 shows the inverse magnetic susceptibility, χ^{-1}, normalized to a gram atom of nickel, plotted against temperature $T \leqslant 300$ K for $x = 0.25$, 0.5 and 0.75. All samples exhibit a Curie–Weiss behaviour at high temperatures with a Curie constant approaching that for an $S = \frac{1}{2}$ state on the Ni(III) ions. The Weiss constant changes from a positive value, $\theta \approx 35$ K, for $x = 0.25$ to negative values of -50 K and -430 K for $x = 0.5$ and $x = 0.75$, respectively.

Room-temperature ESR spectra for $x = 0.05$, 0.25 and 0.5 samples are compared in figure 5 with that reported by Demazeau *et al* (see inset) for ordered $La_2Li_{0.5}Ni_{0.5}O_4$. In the latter compound, the g-factors for the trivalent nickel are strongly anisotropic: $g_\perp = 2.278$ and $g_\parallel = 2.040$. In the $x = 0.25$ sample, $g_\perp = 2.18$ and $g_\perp = 2.01$ are found: the $x = 0.05$ spectrum exhibits a shoulder indicative of orthorhombic symmetry with $g_\perp = 2.20$, $g_2 = 2.16$ and $g_\parallel = 2.03$. A weak signal near $g = 4$ appears in both $x = 0.05$ and $x = 0.25$

Table 1. Activation energy and Seebeck coefficient values of $LaSrB_{1-x}B'_xO_4$ (B, B' ≡ Al, Fe and Ni: B ≠ B').

Composition	x	E_a (eV) $T > T_b$	E_a (eV) $T < T_b$	T_b	α(300 K) (μV K^{-1})
$LaSrAl_{1-x}Ni_xO_4$					
	0.25	—	—	—	+22.0
	0.50	0.290	0.146	238	+38.0
	0.75	0.132	0.07	200	−21.0
	1.00	0.090	0.03	300	−6.6
$LaSrFe_{1-x}Ni_xO_4$					
	0.20	—	0.13	340	+88.79
	0.50	—	0.09	357	+29.96
	0.60	—	—	—	+6.00
	0.80	—	0.064	400	−3.00
	1.00	—	0.03	300	−6.5

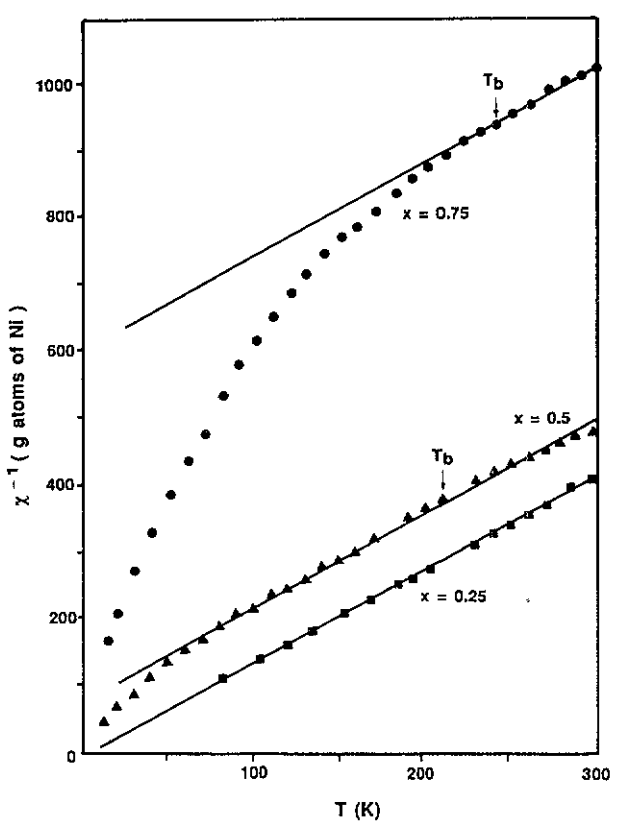

Figure 4. χ^{-1} versus temperature plots of $LaSrAl_{1-x}Ni_xO_4$ compounds.

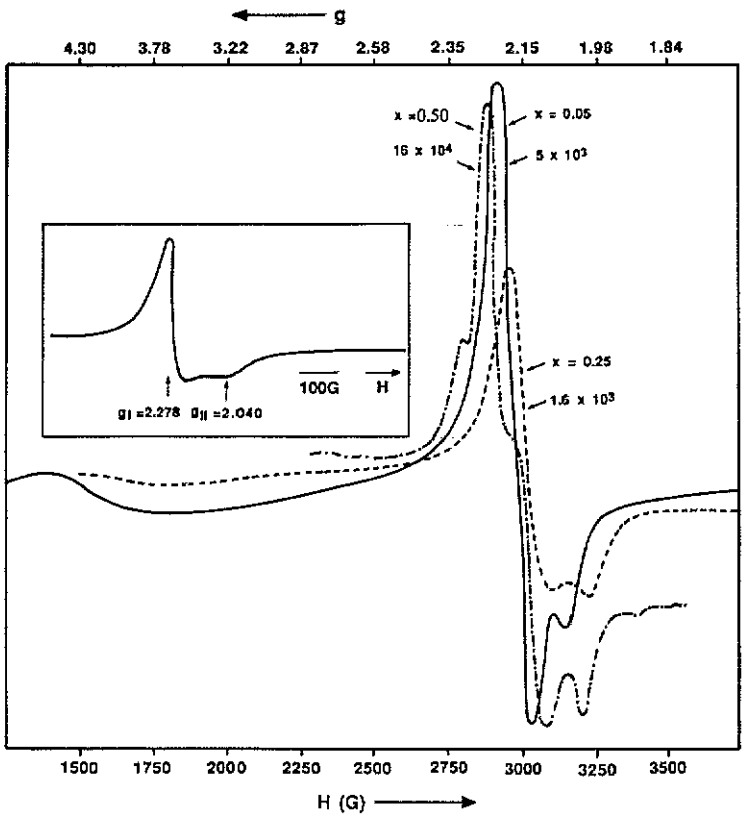

Figure 5. X-band ESR spectra of some members of the $LaSrAl_{1-x}Ni_xO_4$ family at 9.04 GHz frequency. The features of the spectra are not seen clearly for the region near $g = 4.0$. Receiver gains are shown against each curve. In the inset the ESR spectrum obtained by Demazeau *et al* [6] from $La_2Li_{0.5}Ni_{0.5}O_4$ is given.

spectra; a similar observation has been reported by Reinen *et al* [7] and by Demazeau *et al* [8]. The ESR spectrum for the $x = 0.5$ sample is weaker and quite complex. No ESR signal was obtained from the $x = 0.75$ and $x = 1.0$ samples.

3.2. $LaSrFe_{1-x}Ni_xO_4$

As shown in figures 2(*b*)(i) and 2(*b*)(ii), the room-temperature lattice parameters and c/a ratio for the system $LaSrFe_{1-x}Ni_xO_4$ are well behaved in the interval $0 \leqslant x \leqslant 0.8$, but the parameters for $x = 1.0$ do not correspond to an extrapolation of Végard's law obtained for $0 \leqslant x \leqslant 0.8$.

In this system also the temperature dependence of the logarithm of the resistivity (figure 6) yields a change in activation energy E_a at a break temperature T_b; the low-temperature values of E_a, which are compared in table 1 with the high-temperature values, are seen in figure 2(*b*)(iii) to decrease linearly with increasing x throughout the range $0 \leqslant x \leqslant 1$, and the Seebeck coefficient α changes continuously from a positive to a negative value at an $x > x_c$.

Figure 7 shows the inverse molar magnetic susceptibility, χ_m^{-1}, versus temperature for compositions in the system $LaSrFe_{1-x}Ni_xO_4$. A Curie–Weiss law with a negative

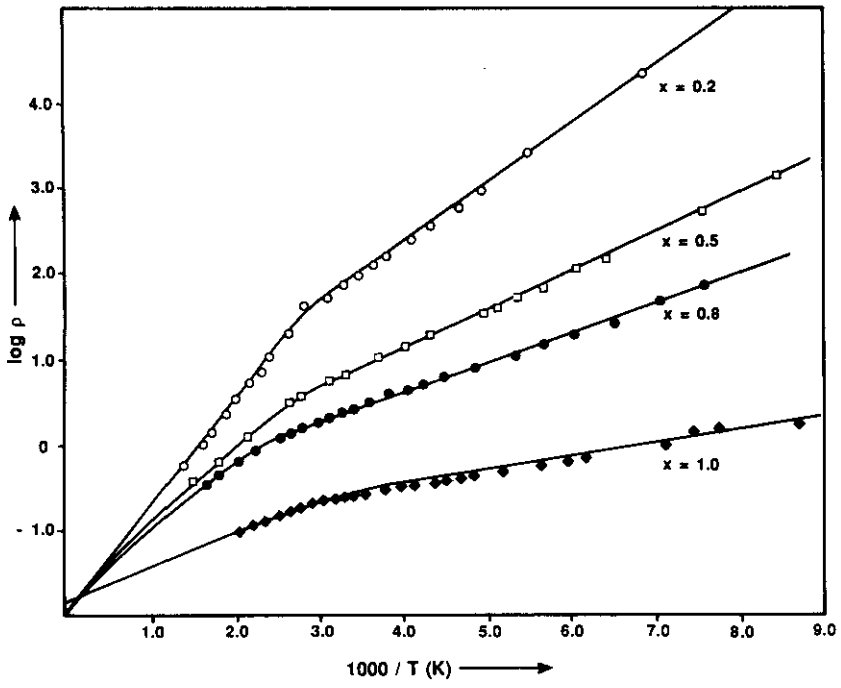

Figure 6. log ρ versus $100/T$ plots of $LaSrFe_{1-x}Ni_xO_4$.

Weiss constant of large magnitude is found above room temperature; the values of μ_{eff} and $|\theta|$ obtained from the straight-line portions of the graph are given in table 2. The observed μ_{eff} is, in every case, a little higher than that calculated μ_{spin} for low-spin Ni(III) and high-spin Fe^{3+} ions. Of particular interest is the lack of any clear evidence for long-range magnetic order in $LaSrFe_{0.8}Ni_{0.2}O_4$ above 20 K: there is only a small dip in the χ_M^{-1} versus T plot in the interval $80\ K < T < 140\ K$. There were problems with disproportionation of intermediate compositions in the system $LaSrFe_{1-x}Ni_xO_4$; a magnetic second phase would then be detected even though no second phase was evident in the x-ray diffraction pattern.

3.3. $LaSrAl_{1-x}Fe_xO_4$

Substitution of the spherically symmetric high-spin Fe^{3+} ion for Al^{3+} is normally straightforward, and indeed the lattice parameters of the system $LaSrAl_{1-x}Fe_xO_4$ increase systematically with the Fe concentration x (figure 8). However, a small deviation from Végard's law is apparent; it is opposite to that expected from non-stoichiometry due to partial reduction of Fe^{3+} to Fe^{2+}. Moreover, the c/a ratio decreases with increasing x.

The reciprocal molar susceptibility versus temperature (figure 9) exhibits a Curie law above 77 K for $x = 0.2$ with $\mu_{eff} \simeq 5.1\ \mu_B$ per iron atom, which is somewhat smaller than the theoretical value of 5.9 μ_B for the $L = 0$, $S = \frac{5}{2}$ ground state of high-spin Fe^{3+}. The data for $x = 0.5$ suggests a Curie–Weiss law above 300 K extrapolating to a large negative Weiss constant (−100 K) due to antiferromagnetic Fe–O–Fe interactions, but with no clear evidence of long-range magnetic order at lower temperatures. The $x = 0.8$ sample exhibits an anomaly indicative of long-range magnetic order below 300 K. It is

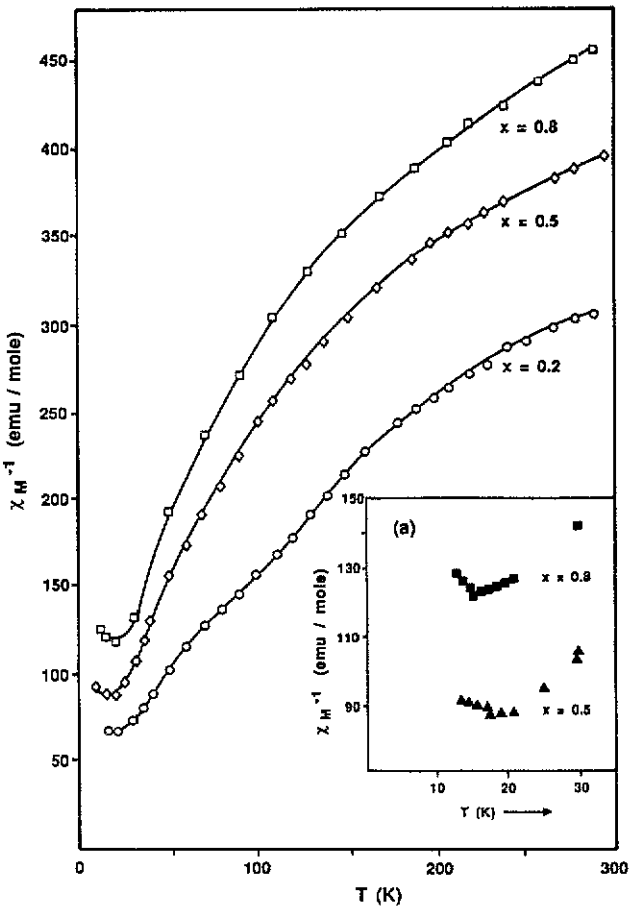

Figure 7. χ_M^{-1} versus T plots of $LaSrFe_{1-x}Ni_xO_4$ at $T < 30$ K. The inset shows the χ_M^{-1} versus T plots in the temperature range 12–30 K of $LaSrFe_{1-x}Ni_xO_4$ ($x = 0.5$ and 0.8).

Table 2. Magnetic susceptibility parameters of $LaSrFe_{1-x}Ni_xO_4$ compounds.

x	Temperature range (K)	$\lvert\theta\rvert$ (K)	μ_{eff} observed (μ_B)	μ_{spin} calculated (μ_B)
0.2	>300	1350	5.89	5.50
0.6	>300	1000	4.82	4.71
0.8	>300	600	3.71	3.10

like that found by Aso and Mihihara [9] for $LaSrFeO_4$, but unlike that found by Soubeyroux *et al* [10] for the same nominal composition (see insets of figure 9).

The room-temperature ESR (figure 10) show a broad line with $g \simeq 2.0$ for all compositions studied; it is asymmetric in the spectrum for $x = 0.02$, which also reveals a complexity that is not observed in the other spectra.

Table 3. Mössbauer parameters for Fe(III) cations in $LaSrFe_{0.8}Ni_{0.2}$ and $Sr_2Fe_{0.5}Ta_{0.5}O_4$ compounds.

Sample	$(IS)_1$ (mm s^{-1})	Δ_1 (mm s^{-1})	Γ_1 (mm s^{-1})	$(IS)_2$ (mm s^{-1})	Δ_2 (mm s^{-1})	Γ_2 (mm s^{-1})
$LaSrFe_{0.8}Ni_{0.2}O_4$	0.523 ± 0.02	1.175 ± 0.05	0.418 ± 0.02	0.682 ± 0.02	0.877 ± 0.05	0.271 ± 0.02
$Sr_2Fe_{0.5}Ta_{0.5}O_4$	0.293 ± 0.02	0.559 ± 0.05	0.212 ± 0.02	0.575 ± 0.02	0.429 ± 0.05	0.212 ± 0.02

3.4. Other comparisons

The room-temperature ^{57}Fe Mössbauer spectra of the compounds $LaSrFe_{0.8}Ni_{0.2}O_4$, $Sr_2Fe_{0.5}Ta_{0.5}O_4$ and $LaSrAl_{0.2}O_4$ are compared in figure 11. All the spectra exhibit asymmetric quadrupole splitting with a broader higher-energy transition. No attempt was made to fit the spectrum of the nominal $LaSrAl_{0.2}Fe_{0.8}O_4$ sample, which was of a poorer quality even though the number of counts was the same as that for the other samples.

In the compound $Sr_2Fe_{0.5}Ta_{0.5}O_4$, an ordering of Fe^{3+} and Ta^{5+} ions with a basal plane was expected. However, this ordering does not appear to be complete; it proved necessary to fit the asymmetric spectrum with two iron species, each with a different isomer shift (IS) and quadrupole splitting Δ (table 3).

Extrinsic conduction in a disordered transition-metal oxide is generally best described by a variable-range hopping; in this regime, $\log \rho$ varies at $T^{-1/4}$ for three-dimensional conduction and at $T^{-1/3}$ for two-dimensional conduction. Figure 12 shows the low-temperature plots of $\log \rho$ versus $T^{-1/4}$ and $T^{-1/3}$ for several samples.

4. Interpretation

4.1. End members

A measure of the A—O and M—O bond-length mismatch across the interfaces between $(AO)_2$ and MO_2 intergrowths in an A_2MO_4 oxide with the tetragonal structure in figure 1 is given by the tolerance factor

$$t = (A—O)/\sqrt{2}(M—O) \tag{1}$$

where A—O and M—O are the mean equilibrium bond lengths in a normal oxide for ninefold-coordinated A cations and octahedrally coordinated M cations. A $t = 1$ corresponds to a perfect bond matching. A $t < 1$ places the M—O bonds under compression, and the A—O bonds under tension. Such a mismatch may be relieved by a cooperative rotation of the MO_6 octahedra about a [110] direction so as to bend the M—O—M bond angles; the rotation lowers the symmetry to orthorhombic as found for room-temperature La_2NiO_4 and La_2CuO_4 [5, 11]. A $t > 1$ places the M—O bonds under tension, and the A—O bonds under compression. In this case, the M—O—M bonds must remain unbent; relief of the internal stresses therefore requires an adjustment of the atomic positions in the $(AO)_2$ layer. A shifting of the cations and anions of the $(AO)_2$ rocksalt layers along the c axis in opposite directions from any one AO plane would provide the required adjustment. Such a shift would manifest itself as an increase in the axial ratio c/a of the tetragonal structure.

At room temperature, the tolerance factor for an oxide is traditionally obtained by setting A—O and M—O bond lengths equal to the sum of the empirical ionic radii for

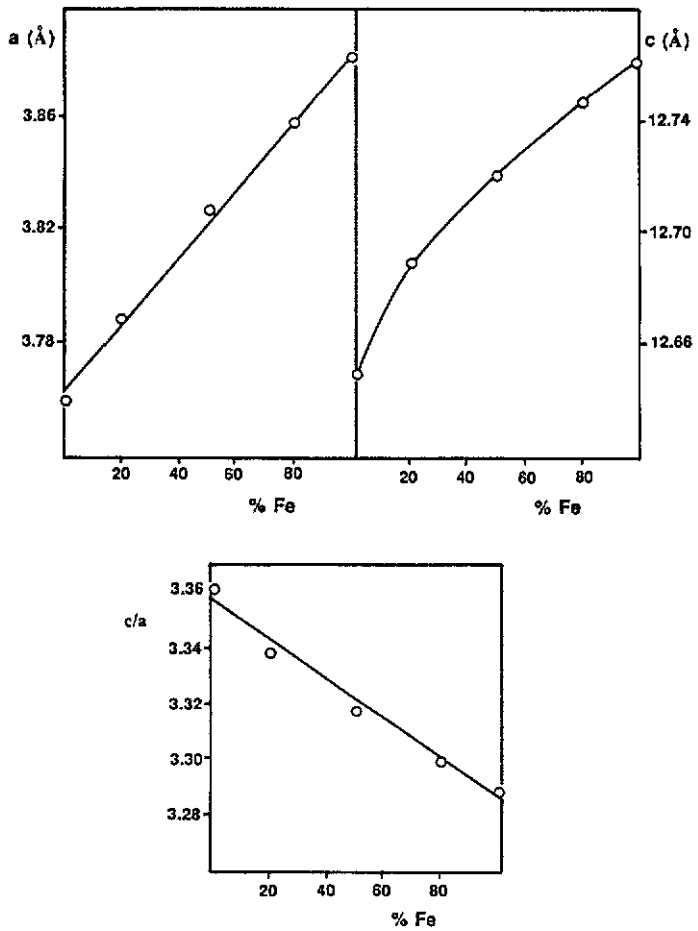

Figure 8. Variation in structural parameters (a, c and c/a) as a function of x in the series $LaSrAl_{1-x}Fe_xO_4$.

the ions. Such a procedure is useful in any consideration of the room-temperature properties; however, it masks the fact that t is temperature dependent because of the different thermal expansion coefficients for the A—O and M—O bond lengths [4, 5]. The structural data for this study were confined to room temperature; it may prove necessary to consider the temperature dependence of t in any quantitative interpretation of the temperature dependence of the physical properties.

The end member $LaSrAlO_4$ is an insulator, transparent to visible light. A room-temperature tolerance factor $t \simeq 1.02 > 1$ is consistent with the observation of a relatively large c/a axial ratio of 3.36 compared with that in the end member $LaSrFeO_4$ where $c/a = 3.28$ reflects a smaller room-temperature tolerance factor $t \simeq 0.97$. Both Al^{3+} and high-spin Fe^{3+} are spherically symmetric ions, but only the Fe^{3+} ion carries a magnetic moment and exhibits a strong antiferromagnetic Fe–O–Fe interaction like that found in the antiferromagnetic perovskite $LaFeO_3$ [12].

Demazeau *et al* [13] have shown, from magnetic and electrical studies, that $LaSrNiO_4$ contains low-spin Ni(III) ions with Ni–O–Ni interactions in the basal planes that are

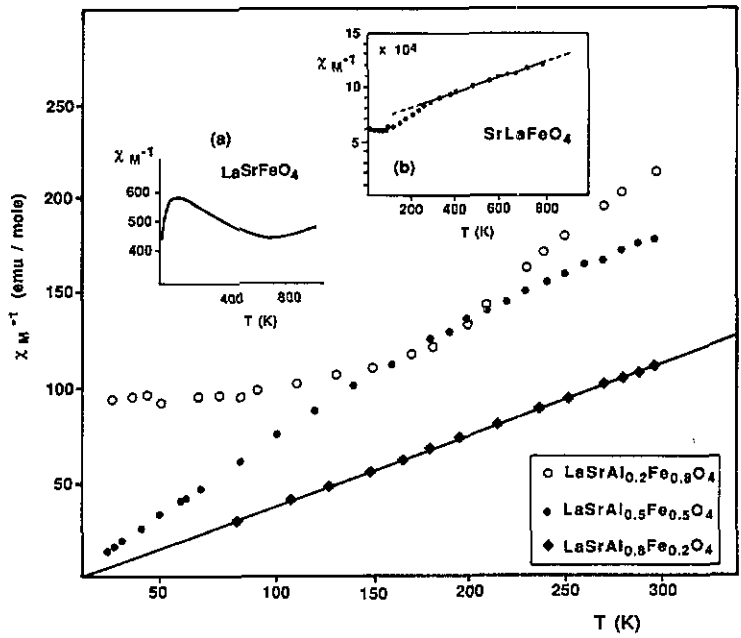

Figure 9. χ_M^{-1} versus T plots of $LaSrAl_{1-x}Fe_xO_4$. The inset show the χ_M^{-1} versus T plots of $LaSrFeO_4$ obtained from the literature: (*a*) by Soubeyroux *et al* [10]; (*b*) by Aso and Mihihara [9].

strong enough to transform the unpaired $d_{x^2-y^2}$ electron on the nickel from a localized to a narrow-band character. Such a situation is analogous to that in the 'cubic' perovskite $LaNiO_3$ [12]; however, it implies that the e-orbital degeneracy has been lifted so as to stabilize the narrow-band electrons in $\sigma^*_{x^2-y^2}$ bands of Ni $3d_{x^2-y^2}$ parentage, where z is taken parallel to the c axis. Such an ordering of the electrons into in-plane orbitals would increase the Ni–O–Ni equilibrium separation, thereby decreasing t and hence the c/a ratio; $c/a = 3.28$ for $LaSrNiO_4$ like that for $LaSrFeO_4$ despite the larger ionic size of high-spin Fe^{3+} is therefore consistent with such an ordering.

4.2. $LaSrAl_{1-x}Ni_xO_4$ versus $LaSrAl_{1-x}Fe_xO_4$

The Al^{3+} ion is a main-group element having no energetically accessible 3d orbitals. The large band gap in $LaSrAlO_4$ is a measure of the separation between the Al 3s conduction band and the O^{2-} $2p^6$ valence band. With the initial introduction of an isolated transition-metal atom Ni(III) or Fe^{3+}, only Ni–O–Al or Fe–O–Al interactions are present. In this situation the 3d electrons at the transition-metal atoms remain localized in crystal-field orbitals (atomic orbitals hybridized with appropriately symmetrized oxygen orbitals). The situation is analogous to that found in the ordered compound $La_2Li_{0.5}Ni_{0.5}O_4$, where there are ideally only Li–O–Ni interactions in an $M_{0.5}M'_{0.5}O_2$ plane; in this compound the low-spin Ni(III) configuration is localized and the nickel atoms carry a moment of $1\mu_B$ in a paramagnetic insulator [6].

On the other hand, where the charges on the two M cations are similar, such an ordering is not anticipated; M–O–M interactions between the transition-metal M atoms

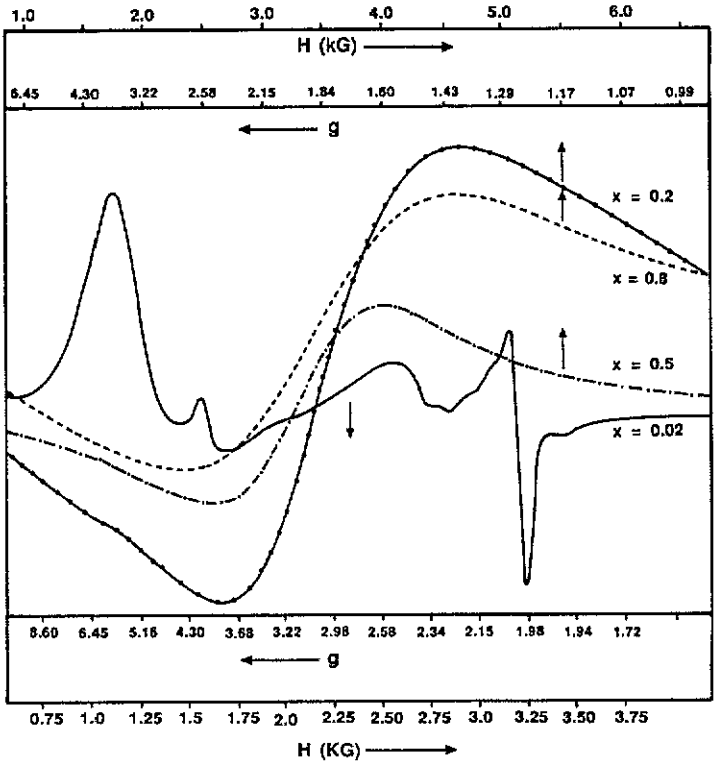

Figure 10. X-band ESR spectrum of $LaSrAl_{1-x}Fe_xO_4$ ($x = 0.02, 0.2, 0.5$ and 0.8).

increase in number with increasing concentration x of the M atom. For a two-dimensional square net, classical percolation theory with only nearest-neighbour interactions gives a percolation threshold $x_c \simeq 0.59$ [14] compared with $x_c \simeq 0.31$ for the simple-cubic array [15] applicable to a cubic perovskite. The fact that the physical properties of the system $LaSrAl_{1-x}Ni_xO_4$ (shown in figure 2(*a*)) changes rapidly with x in the interval $0.5 < x < 0.75$ is therefore taken as a manifestation of changes occurring on crossing the percolation threshold $x = x_c \simeq 0.59$. A similar anomaly is not found in the system $LaSrAl_{1-x}Fe_xO_4$; so we conclude that the changes occurring in the nickel system are associated with rearrangements of the ordering of the e electron among the possible e orbitals and that these rearrangements are induced by Ni–O–Ni interactions; the stable e-orbital configuration varies with the number of Ni–O–Ni interactions available to a Ni atom.

If a Ni atom has only Al nearest neighbours, the oxygen of an Al–O–Ni band is polarized towards the Ni and away from the Al to yield a relatively strong covalent mixing between Ni $3d_{x^2-y^2}$ and O $2p\sigma_x$, $2p\sigma_y$ orbitals. A similar polarization of the *c*-axis oxygen away from the La or Sr *c*-axis neighbour towards the Ni atoms is weakened at low concentrations by a tolerance factor $t > 1$ that increases the *c*-axis Ni–O separation. Therefore, for smaller x, we may assume that the Ni $3d_{x^2-y^2}$ orbitals are raised above the Ni $3d_{z^2}$ orbitals; so the unpaired electron at a Ni(III) ion occupies the $3d_{z^2}$ orbital parallel to the *c* axis. Since it is an antibonding electron, the local octahedral site is distorted to tetragonal ($c/a > 1$) symmetry. A similar ordering of the 3d electrons is not

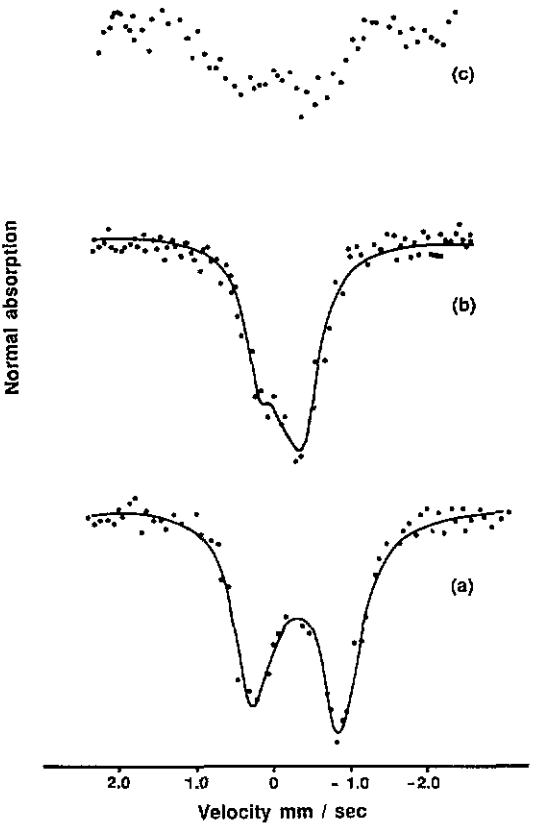

Figure 11. Mössbauer spectrum of (*a*) $LaSrFe_{0.8}Ni_{0.2}O_4$, (*b*) $Sr_2Fe_{0.5}Ta_{0.5}O_4$ and (*c*) $LaSrAl_{0.2}Fe_{0.8}O_4$.

possible on high-spin Fe^{3+}, which has every 3d orbital occupied by one electron. These differences manifest themselves in the variations in c/a ratio with x in figures 2(*a*) and 8.

In figure 8 the axial ratio decreases nearly linearly with increasing x; the decrease is consistent with a decreasing t, and the deviation from a straight line reflects, at least in part, an increasing net Fe–O–Fe attractive magnetic interaction (an exchange striction) within the basal planes. In figure 2(*a*), the axial ratio decreases with increasing x much more slowly at small x, accelerating sharply on passing through a transition on crossing the percolation threshold. In the region $0.75 \leqslant x \leqslant 1.0$, the Ni $3d_{x^2-y^2}$ orbitals clearly lie lower than the Ni $3d_{z^2}$ orbitals as in the end member $LaSrNiO_4$. The crossover in the relative energies of the $3d_{x^2-y^2}$ and $3d_{z^2}$ orbitals is apparently induced by the introduction of Ni–O–Ni interactions, which weaken an individual Ni–O covalent mixing because an O $2p_\sigma$ orbital becomes shared by two Ni atoms. As the number of Ni–O–Ni interactions increases and of the Ni–O–Al interactions decreases, the stable 3d orbital need not change abruptly from $3d_{x^2-y^2}$ to $3d_{z^2}$; it may occur via some intermediate such as $3d_{z^2-x^2}$, $3d_{z^2-y^2}$, or an orthorhombic orbital; it is therefore interesting that the transition from predominantly $3d_{x^2-y^2}$ to predominantly $3d_{z^2}$ character appears to be sharp. A sharp transition at the percolation threshold may well reflect a transition from a localized to an itinerant character of the σ-bonding electrons.

The other physical properties vary with x in a manner consistent with this interpretation. In the $LaSrAl_{1-x}Ni_xO_4$ system, the slope of the inverse susceptibility versus

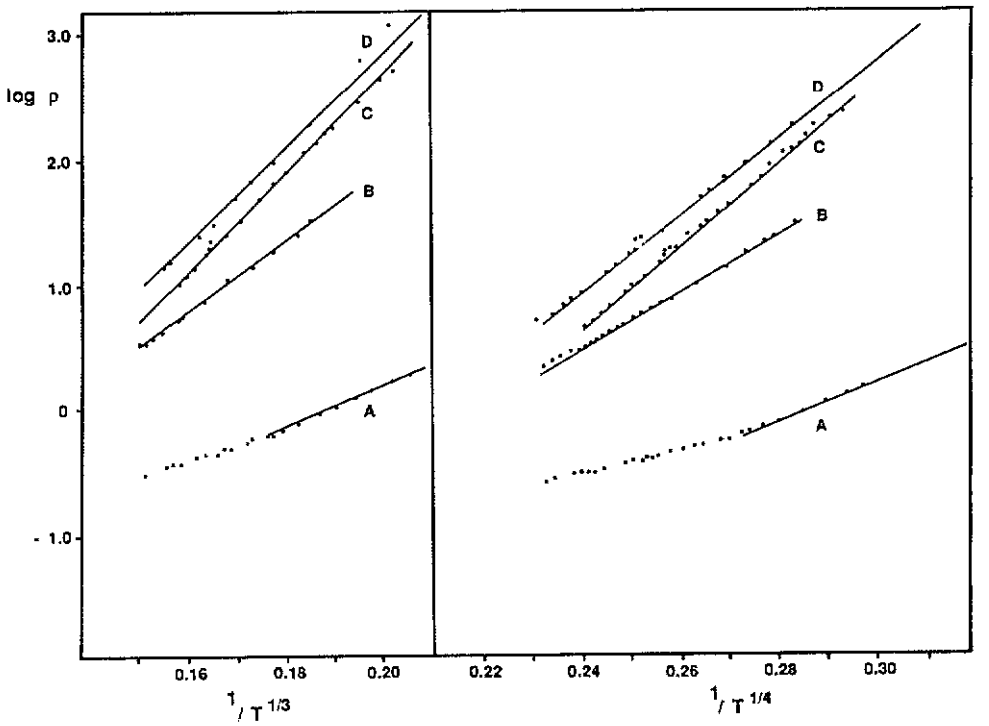

Figure 12. (*a*) log ρ versus $T^{-1/3}$ and (*b*) log ρ versus $T^{-1/4}$ plots for $LaSrNiO_4$ (lines A), $LaSrFe_{0.2}Ni_{0.8}O_4$ (lines B), $LaSrAl_{0.25}Ni_{0.75}O_4$ (lines C) and $LaSrFe_{0.5}Ni_{0.5}O_4$ (lines D).

temperature and the ESR data confirm the presence of the localized $S = \frac{1}{2}$ state at low-spin Ni(III) ions for all $x \leqslant 0.75$. A positive Weiss constant for $x = 0.25$ indicates that ferromagnetic Ni–O–Ni interactions are dominant where the nickel e electrons predominantly occupy $3d_{x^2-y^2}$, or $3d_{z^2-y^2}$ orbitals. For a Ni–O–Ni interaction along the x axis, it is possible to envisage a dynamic fluctuation of $d^1_{z^2-x^2}$–O $2p\sigma_x$–$d^0_{x^2-y^2}$ and $d^0_{x^2-y^2}$–O $2p\sigma_x$–$d^1_{z^2-y^2}$ configurations associated with x-axis optical-mode vibrations; such fluctuations would give a ferromagnetic superexchange interaction via the dynamic coupling of a half-filled with an empty orbital [16]. However, as the concentration of Ni–O–Ni interactions increases, more and more static $d^1_{z^2-x^2}$ configurations become stabilized; by $x = 0.5$, a negative Weiss constant signals that the antiferromagnetic Ni–O–Ni superexchange interactions dominate the dynamic ferromagnetic interactions. A crossover to predominantly $d^1_{x^2-y^2}$ configurations for $x \geqslant 0.75$ introduces strongly antiferromagnetic Ni–O–Ni interactions that are two dimensional in character; so the magnetic order is short range. The susceptibility for $x = 0.8$ (inset of figure 7) is difficult to interpret unambiguously; the magnitude of the nickel moment appears to be suppressed, but there may be long-range antiferromagnetic order below 50 K.

In the $LaSrAl_{1-x}Fe_xO_4$ systems, the ESR and magnetic susceptibility data indicate that some loss of oxygen has occurred, which would create Fe^{2+} ions trapped at oxygen vacancies. Since small-polaron formation would introduce an activation energy into any ferromagnetic double-exchange interaction, thereby suppressing it, any magnetic interactions should be dominated by strong antiferromagnetic Fe–O–Fe superexchange

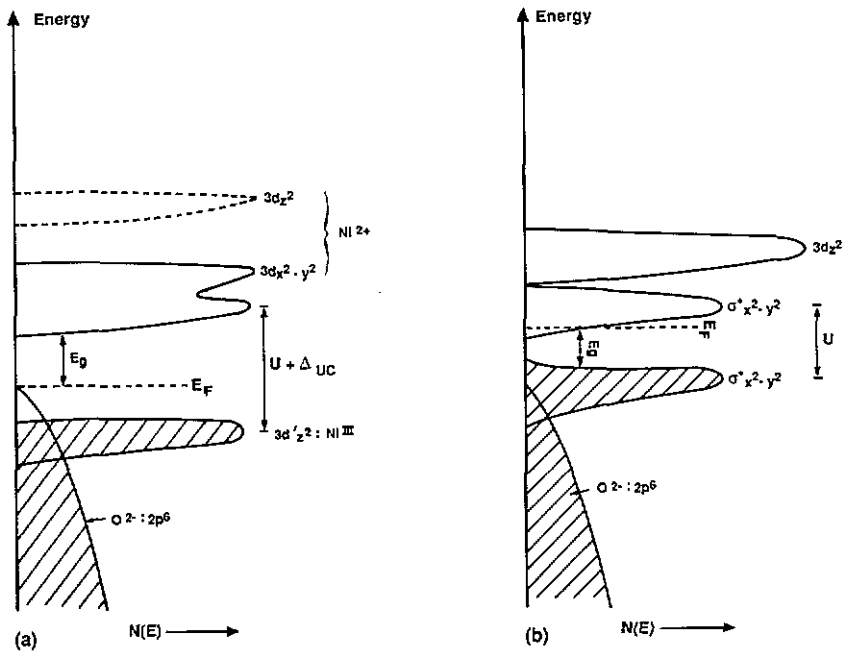

Figure 13. Semi-empirical energy band diagram of $LaSrAl_{1-x}Ni_xO_4$: (*a*) $x < 0.6$; (*b*) $x > 0.6$.

interactions. Nevertheless, an $x = 0.2$ sample shows a zero Weiss constant, and there is no evidence of long-range antiferromagnetic order at $x = 0.5$, which is below the percolation threshold $x_c \simeq 0.59$; however, there is long-range magnetic order for $x \geqslant 0.8$. These data suggest at least some preference for Al^{3+} as near neighbours of Fe^{3+} for $x = 0.2$.

Discussion of the transport data for the system $LaSrAl_{1-x}Ni_xO_4$ begins with the qualitative energy diagram in figure 13, which depicts in figure 13(*a*) the localized Ni 3d crystal-field energies associated with dilute concentrations x. Strong hybridization of the Ni 3d and O 2p orbitals is present in the crystal-field orbitals, which reduces the correlation energy U splitting the filled Ni(*III*) configuration and the empty Ni^{2+} configuration, but not the non-cubic part of the crystal-field splitting Δ_{nc} that stabilizes a Ni(III) $3d^1_{z^2}3d^0_{x^2-y^2}$ configuration relative to a Ni(III) $3d^1_{x^2-y^2}3d^0_{z^2}$ configuration. In this limit the Ni^{2+} energies act as acceptor states, and the mobile charge carriers are holes in the strongly hybridized valence band of O 2p and Ni 3d states. The result is a positive Seebeck coefficient. The charge is activation energy E_a at $T = T_b$ implies a small excess concentration of oxygen in the structure, which would lower E_F to the top of the valence band at the lowest temperatures. Anderson localization at the top of the band due to the Ni–Al mix results in variable-range hopping. $E_a \simeq 0.3$ eV for $T > T_b$ would correspond to a Ni^{2+} energy located about 0.6 eV above the top of the valence band.

The shape of the variation in α with x in figure 2(*a*) indicates that the oxygen stoichiometry changes with decreasing tolerance factor t from a slight excess to a small deficiency as the percolation threshold $x_c = 0.59$ is crossed; at the same time the crossover of $3d_{z^2}$ and $3d_{x^2-y^2}$ energies signalled by the structural changes allows electron mobility within the MO_2 sheets via a narrow Ni–O–Ni band $\sigma^*_{x^2-y^2}$. The $\sigma^*_{x^2-y^2}$ band had

classical Anderson localization at the band edges because of perturbations introduced by the Al atoms. Variable-range hopping dominates for $T < T_b$. Broadening of the $\sigma^*_{x^2-y^2}$ band with increasing x reduces the correlation splitting and hence the intrinsic energy gap between filled and empty $\sigma^*_{x^2-y^2}$ bands; an effective gap of 0.25 eV appears reasonable as the narrow-band limit is approached. The semi-empirical energy band diagram for $x > 0.6$ is shown in figure 13(*b*). The correlation splitting of the $\sigma^*_{x^2-y^2}$ band, and hence the intrinsic energy gap, decreases with increasing x.

Finally, the ESR spectra of the $LaSrAl_{1-x}Fe_xO_4$ system are consistent with the presence of oxygen vacancies; the broad line with $g \simeq 2.0$ (figure 10) is typical for oxygen vacancies containing a single trapped electron. The complexity of the spectrum for $x = 0.02$ and that for $x = 0.05$ in $LaSrAl_{1-x}Ni_xO_4$ may reflect local changes in the *c*-axis positions of the rocksalt layer atoms, which appear to be displaced at room temperature by $t > 1$ $LaSrAlO_4$ as judged by the relatively large c/a axial ratio.

4.3. $LaSrFe_{1-x}Ni_xO_4$

In the $LaSrFe_{1-x}Ni_xO_4$ system, the Fe–O–Ni interactions appear to be strong enough to stabilize the unpaired electron at a Ni(III) ion in orbitals that are primarily $3d_{x^2-y^2}$ for all x. Consequently the lattice parameters change smoothly with x across $x_c \simeq 0.59$ for $0 \leqslant x \leqslant 0.8$. The small anomalous contraction of the c/a axial ratio for $x = 1.0$ appears to be a real effect that is associated with the elimination of magnetic Ni^{2+} ions.

This latter assertion is supported not only by the magnetic data in figure 7 but also by the observation that the lattice parameters for $0.2 \leqslant x \leqslant 0.8$ varied sensitively with the method of preparation. A prolonged (several days) anneal in oxygen at 1170 K after an initial firing at 1470 K proved necessary to obtain a proper (within 0.5%) oxygen stoichiometry and a systematic lattice parameter variation with x. The lattice parameters in figure 2(*b*) were obtained after this thermal treatment. A sensitivity of the lattice parameters to the oxygen stoichiometry follows from the fact that the equilibrium reaction

$$Fe^{2+} + Ni(III) \leftrightarrow Fe^{3+} + Ni^{2+}$$

is shifted strongly to the right. A magnetic Ni^{2+} ion in an octahedral site has no orbital degeneracy and therefore cannot adapt the spatial distribution of its σ-antibonding electron density to optimize its potential energy. On the other hand, crossover to a low-spin configuration at a Ni(II) ion as a result of strong Ni–O–Ni interactions that reduce U for the $\sigma^*_{x^2-y^2}$ band, leaving an empty $3d_{z^2}$ orbital above the Fermi energy E_F as illustrated in figure 14(*b*).

Support for stabilization of the unpaired electron per low-spin Ni(III) ion in an orbital that is primarily $3d_{x^2-y^2}$ also comes from the magnetic data in figure 7. According to the rules for the superexchange interactions [16], the evidence for strong antiferromagnetic Fe–O–Fe, Fe–O–Ni and Ni–O–Ni interactions for all $0 \leqslant x \leqslant 0.8$ can only be reconciled with half-filled $d_{x^2-y^2}$ orbitals at both Fe^{3+} and Ni(III) ions. The lack of long-range antiferromagnetic order above 20 K is attributable to the two-dimensional character of the magnetic coupling.

Interpretation of the transport properties begins with the semi-empirical energy diagram in figure 14. The Fe^{3+} $3d^5$ and Ni(III) $3d^7$ configurations lie close to the top of the O^{2-} $2p^6$ band; the Fe^{2+} $3d^6$ level lies nearly 3.0 eV above it because of the strong electron correlation energy associated with the addition of a sixth electron to a high-spin

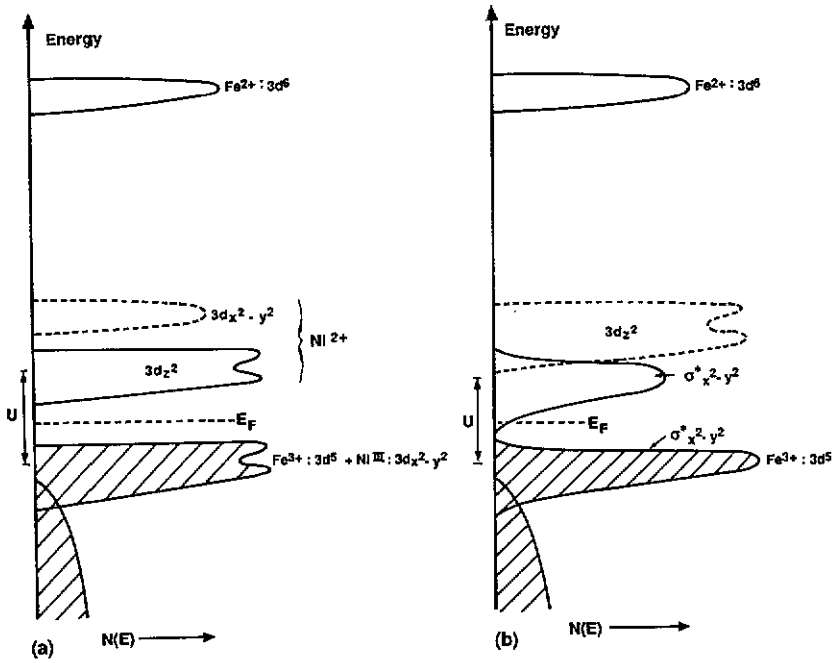

Figure 14. Semi-empirical energy band diagram of $LaSrFe_{1-x}Ni_xO_4$: (*a*) $x < 0.5$; (*b*) $x > 0.5$.

$3d^5$ configuration. The Ni^{2+} $3d^8$ level, on the other hand, lies only about 0.5 eV above Fe^{3+} $3d^5$ level [17], which makes energetically accessible the charge transfer reactions

$$Fe^{3+} + Ni(III) \rightarrow Fe^{4+} + Ni^{2+}$$

$$Ni(III) + Ni(III) \rightarrow Ni(IV) + Ni^{2+}.$$

A strong O 2p admixture into the states associated with holes in the Fe^{3+} and Ni(III) energies makes hole transport mobile relative to electron transport, which is restricted to the nickel atom array where it is inhibited for nickel concentrations x below the percolation limit $x_c \simeq 0.59$. It follows that even slightly reduced samples with $x < x_c$ may have room-temperature Seebeck coefficients $\alpha > 0$ as observed (figure 2(*b*)). For $x > x_c$, electron conduction may dominate to yield $\alpha < 0$, as is also observed. The transition from $\alpha > 0$ to $\alpha < 0$ in figure 2(*b*) contrasts markedly with that in figure 2(*a*); this difference is compatible with slightly reduced samples and an ordering of the unpaired electron at Ni(III) into orbitals of predominantly $3d_{x^2-y^2}$ parentage for all values of x in $LaSrFe_{1-x}Ni_xO_4$.

According to figure 14, all the iron should be present as Fe^{3+} ions in the system $LaSrFe_{1-x}Ni_xO_4$. Therefore we interpret the large anisotropic quadrupole splitting in the Mössbauer spectrum in figure 11 to be a manifestation of the highly anisotropic character of the interatomic exchange interactions at the Fe^{3+} ions. Strong Fe–O–Fe and Fe–O–Ni interactions within the basal planes contrast with weak Fe–O–O–Fe, Ni interactions between planes; this two-dimensional exchange produces the strong quadrupole splitting that is observed. An asymmetric quadrupole splitting may be caused by an axial exchange field within the basal plane. An axial field can give rise to a

Goldanski–Karyagin effect [18] due to anisotropic recoilless fractions and, more important, to the slowing down of the spin–spin relaxation rate via population at higher temperatures of the higher-energy doublets $\pm\frac{3}{2}$ and $\pm\frac{5}{2}$ of the axial-field split $S = \frac{5}{2}$ state at an Fe^{3+} ion. Blume [19] has argued that this latter effect causes the higher-energy line of a quadrupole doublet, which corresponds to $\pm\frac{3}{2} \rightarrow \pm\frac{1}{2}$ transitions, to become more broadened than the line corresponding to $\pm\frac{1}{2} \rightarrow \mp\frac{1}{2}$ and $\pm\frac{1}{2} \rightarrow \mp\frac{3}{2}$ transitions.

In the compound $Sr_2Fe_{0.5}Ta_{0.4}O_4$ on the other hand, incomplete ordering of the Fe^{3+} and Ta^{5+} ions gives rise to two distinguishable isomer shifts and quadrupole splitting (see table 3). Interchange of an Fe with a Ta near neighbour in a basal plane creates an isolated Fe–O–Fe–O–Fe triple. Reduction introduces, in this case, an Fe^{2+} ion within a triple, and a charge transfer within such a triple that is fast relative to 10^{-8} s creates an isomer shift with respect to elemental Fe that is given by the empirical formula [20]

$$IS_m = (2.85 - 0.85 \pm 0.1)\ \text{mm s}^{-1}$$

for a mean iron valence Fe^{m+}. According to this formula, the isomer shift for an isolated Fe^{3+} ion ($m = 3$) would normally be 0.30 ± 0.1 mm s^{-1} and that for a triple that had been reduced by a single, rapidly hopping electron ($m = 2.67$) would be 0.58 ± 0.1 mm s^{-1}. Comparison with table 3 indicates the presence of Fe^{3+} ions and of Fe–O–Fe–O–Fe triples reduced by a single, rapidly hopping electron. Although quadrupole splitting is to be expected from the tetragonal site symmetry, a smaller c/a axial ratio and in-plane Fe–O–Ta–O–Fe interactions reduce its magnitude relative to that found in $LaSrFe_{1-x}Ni_xO_4$. Moreover, only the triples contain an axial field to introduce an anisotropy, and these configurations tend to contain a trapped, rapidly hopping electron.

5. Conclusions

From the preliminary data reported here on $LaSrM_{1-x}M'_xO_4$ with M, M′ ≡ Al, Fe, Ni (but M ≠ M′) the following deductions have been made.

(1) $LaSrAlO_4$ has a room-temperature tolerance factor $t > 1$ and an anomalously large axial ratio c/a. Atomic displacements parallel to the c axis within the rocksalt layers to relieve the compressive stress on these layers would increase c. Neutron diffraction data are needed to confirm whether such displacements are present.

(2) The trivalent ions of Al, Fe and Ni remain distorted within the MO_2 planes of the A_2MO_4 structure in figure 1, but there may be short-range ordering of Fe and Al for smaller x in $LaSrAl_{1-x}Fe_xO_4$.

(3) Ni is present predominantly as low-spin Ni(III). In $LaSrAl_{1-x}O_4$ the d_{z^2} orbital is more stable than the $d_{x^2-y^2}$ orbital for $x = 0$ and less stable for $x = 1$; a sharp crossover and transition from p-type to n-type conductivity occurs near the percolation limit $x_c \simeq 0.59$. In $LaSrFe_{1-x}Ni_xO_4$ the $d_{x^2-y^2}$ orbital is more stable for all x, and a smooth transition from p-type to n-type conduction occurs near x_c. The system $LaSrAl_{1-x}Fe_xO_4$ exhibits long-range antiferromagnetic order only for $x > x_c$.

(4) A small correlation splitting of the narrow $\sigma^*_{x^2-y^2}$ band of Ni $d_{x^2-y^2}$ parentage appears to occur in $LaSrNiO_4$. Substitution of 25 mol% Al or Fe for Ni induces an atomic moment on the Ni atoms; some high-spin Ni^{2+} ions are present as a result of oxygen deficiency. Band tailing introduces localized states in the correlation energy gap.

(5) A break temperature T_b in the log ρ versus $1/T$ plots appears to mark a transition from variable-range hopping to intrinsic conduction with increasing T, but a change in

electron coupling to the crystallographic vibrational modes cannot be ruled out on the basis of present evidence.

In addition, incomplete ordering of Fe^{3+} and Ta^{5+} in $Sr_2Fe_{0.5}Ta_{0.5}O_4$ leads to the formation of Fe–O–Fe–O–Fe triples that, on reduction, capture electrons in preference to isolated Fe^{3+} ions. Electron hopping within a triple reduced by one electron is $\tau_h < 10^{-8}$ s.

Acknowledgment

We would like to thank the R A Welch Foundation (JBG), British Petroleum (PPE) and SERC (PPE, KKS) for financial support.

Note added in proof. A paper by Benloucif *et al* [21] has recently appeared. This deals with the relationships between oxygen content and electronic structure in $La_{2-x}Sr_xNi_{1-y}Fe_yO_{4-[(x-y)/2]+\delta}$.

References

[1] Iwazumi T, Yoshizaki R, Sawada H, Uwe H, Sakuda T and Matsuurz E 1987 *Japan. J. Appl. Phys.* **26** L386
[2] Maekawa S, Ebisawa H and Isawa Y 1987 *Japan. J. Appl. Phys. Lett.* **26** L468
[3] Hundley M F, Thompson J D, Cheong S-W, Fisk Z and Schirber J E 1990 *Phys. Rev.* B **41** 4062
[4] Goodenough J B 1986 *J. Less-Common Met.* **116** 83
[5] Goodenough J B 1990 *Supercond. Sci. Technol.* **3** 26
[6] Demazeau G, Marty J L, Pouchard M, Rojo T, Dance J M and Hagenmuller P 1981 *Mater. Res. Bull.* **16** 47
[7] Reinen D, Friebel C and Propack V Z 1974 *Z. Anorg. (Allg.) Chem.* **408** 187
[8] Demazeau G, Marty J L, Buffat B, Dance J M, Pouchard M, Dordor P and Chevalier B 1982 *Mater. Res. Bull.* **17** 37
[9] Aso K and Mihihara S 1966 *J. Phys. Soc. Japan* **21** 1833
[10] Soubeyroux J L, Courbin P, Fourmes L, Fruchart D and LeFleur G 1980 *J. Solid State Chem.* **31** 313
[11] Singh K K, Ganguly P and Goodenough J B 1984 *J. Solid State Chem.* **52** 252
[12] Goodenough J B and Longo J M 1970 *Landolt–Börnstein New Series* Group III, vol 4a, ed K H Hellwege (Berlin: Springer) p 126
[13] Demazeau G, Pouchard M, Thomas M, Colombet J-F, Grenier J-C, Fournes L, Soubeyroux J L and Hagenmuller P 1980 *Mater. Res. Bull.* **15** 451
[14] Walsh W M, Birgeneau R J L, Rupp W and Guggenheim M J 1979 *Phys. Rev.* B **20** 4645
[15] Shante B K and Kirkpatrick S 1971 *Adv. Phys.* **20** 325
[16] Goodenough J B, Wold A, Arnott R J and Menyuk N 1961 *Phys. Rev.* **124** 373
[17] Mizushima K, Tanaka M, Asai A, Iida S and Goodenough J B 1979 *J. Phys. Chem. Solids* **40** 1129
[18] Goldanski V I, Gorodinski G M, Markar E F, Suzdaler I P and Khrapov V V 1962 *Dokl. Akad. Nauk* **147** 127
[19] Blume M 1967 *Phys. Rev. Lett.* **18** 305
[20] Gleitzer C and Goodenough J B 1985 *Struct. Bonding (Berlin)* **61** 1
[21] Benloucif R, Nguyen N, Greneche J M and Raveau B 1991 *J. Phys. Chem. Solids* **52** 381